ACS APPLIED MATERIALS & INTERFACES

www.acsami.org Research Article

Bending Strain-Tailored Magnetic and Electronic Transport Properties of Reactively Sputtered γ'-Fe_4N/Muscovite Epitaxial Heterostructures toward Flexible Spintronics

Xiaohui Shi, Mei Wu, Zhengxun Lai, Xujing Li, Peng Gao, and Wenbo Mi*

Cite This: *ACS Appl. Mater. Interfaces* 2020, 12, 27394−27404 Read Online

ACCESS | Metrics & More | Article Recommendations | Supporting Information

ABSTRACT: The strain modulation on the magnetic and electronic transport properties of the ferromagnetic films is one of the hot topics due to the practical applications in flexible and wearable spintronic devices. However, the large strain-induced saturation magnetization and resistance change is not easy to achieve because most of the ferromagnetic films deposited on flexible substrates are polycrystalline or amorphous. Here, the flexible epitaxial γ'-Fe_4N/mica films are fabricated by facing-target reactive sputtering. At a tensile strain with a radius of curvature (ROC) of 3 mm, the saturation magnetization (M_s) of the γ'-Fe_4N/mica film is tailored significantly with a maximal variation of 210%. Meanwhile, the magnetic anisotropy was broadly tunable at different strains, where the out-of-plane M_r/M_s at a tensile strain of ROC = 2 mm is six times larger than that at the unbent state. Besides, the strain-tailored longitudinal resistance R_{xx} and anomalous Hall resistivity ρ_{xy} appear where the drop of R_{xx} (ρ_{xy}) reaches 5% (22%) at a tensile strain of ROC = 3 mm. The shift of the nitrogen position in the γ'-Fe_4N unit cell at different bending strains plays a key role in the strain-tailored magnetic and electronic transport properties. The flexible epitaxial γ'-Fe_4N films have the potential applications in magneto- and electromechanical wearable spintronic devices.

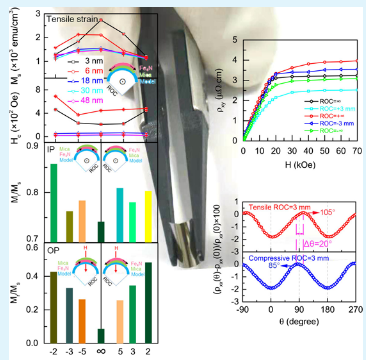

KEYWORDS: *epitaxial γ'-Fe_4N films, magnetic properties, electronic transport properties, nitrogen position, flexible spintronics*

INTRODUCTION

Flexible spintronics combines the conventional spintronics with the advantages of mechanically flexible electronics due to light weight, chemical inertness, thermal conductivity, multi-function, and environmental friendliness.[1−3] Lots of flexible magnetic materials have been widely investigated for wearable spintronic devices, such as the giant magnetoresistance sensors,[4,5] magnetoelectric devices,[1,6] and skin electronics.[7−10] Many methods have been used to produce large strains, which can exert significant effects on magnetic properties, such as dual-ion-tuned electronic structures,[11] depositing films on various substrates,[12] and strain-mediated magnetoelectric coupling effects.[13] In flexible spintronics, the magnetic and electronic transport properties of the ferromagnetic films are mainly tailored via applying the bending strains (>1.0%),[14−19] which is larger than the piezoelectric strain (<0.2%) in $PbZr_xTi_{1-x}O_3$.[20,21] However, the integration of epitaxial films on flexible organic substrates is quite difficult due to the lower fabrication temperatures (<300 °C) and lattice mismatch.[22−25] Meanwhile, the large strain-induced magnetization and resistance change are also not easy to achieve because most of the ferromagnetic films deposited on flexible substrates are polycrystalline or amorphous. The poor lattice symmetry, low anisotropy, and complicated grain boundaries in the polycrystalline or amorphous films, such as flexible polycrystalline $Fe_{81}Ga_{19}$ and amorphous $Co_{40}Fe_{40}B_{20}$ films,[14,26−28] make them have a weaker response to the strains, which can result in a smaller modulation on the magnetic and electronic transport properties than that in the epitaxial films.[1,2] Since, the epitaxial films can effectively transfer the strain from the substrate, the epitaxial ferromagnetic films with a large magnetization, anisotropy magnetoresistance (AMR), and anomalous Hall resistivity are more desirable.[29−31] Meanwhile, the muscovite simplified as "mica" [$KAl_2Si_3AlO_{10}$)$(OH)_2$] has been paid much attention to achieve a large strain due to its large stretchability.[32−34] The melting point of mica is as high as 1300 °C, which is necessary to fabricate the epitaxial ferromagnetic films.[2,15,35,36]

It is noted that the magnetic and electronic transport properties of the flexible epitaxial ferromagnetic films are tightly associated with the applied tensile and compressive strains. In the epitaxial $CoFe_2O_4$/mica heterostructure,[16] the robust magnetic properties at different strains were attributed to randomly distributed upward and downward magnetic

Received: May 1, 2020
Accepted: May 28, 2020
Published: May 28, 2020

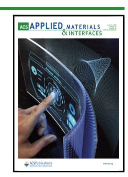

domains despite the existence of a large magnetostrictive behavior of −104 ppm in $CoFe_2O_4$. In the epitaxial $La_{0.67}Sr_{0.33}MnO_3$/mica films,[15] a slight enhancement of saturation magnetization (M_s) at both the compressive and tensile strains was caused by the magnetomechanical coupling effects. In the epitaxial $SrRuO_3$/mica films,[37] the enhancement of M_s and the transformation of magnetic anisotropy from in-plane magnetic anisotropy (IMA) to perpendicular magnetic anisotropy (PMA) were ascribed to the spin state transition induced by the bending strains. By considering the bending-induced strain effects on electronic transport properties, Huang et al. found that the enhanced MR of $La_{0.67}Sr_{0.33}MnO_3$/mica can be ascribed to more grain boundary- or phase boundary-induced spin fluctuation under mechanically bending strains.[15] Moreover, Zheng et al. observed that the Verwey transition temperature of Fe_3O_4/mica increases (decreases) under the compressive (tensile) strains, which was attributed to the charge reconstruction effect at different bending states.[36] Obviously, the bending-induced strain effects on the magnetic and electronic transport properties are complicated in different materials. Meanwhile, the underlying mechanisms of the tailored magnetic properties by the bending-induced strains are still in debate.

Antiperovskite-type cubic γ'-Fe_4N exhibits a high degree of ductility since its bulk modulus B to elastic constant C_{44} (namely B/C_{44}) can reach to 3.4−4.2.[38,39] Specifically, γ'-Fe_4N has a high Curie temperature of 767 K and a large M_s of 1440 emu cm^{-3}, which make it have the wide applications in the magnetic sensing and storage.[39−44] In this work, γ'-Fe_4N with high ductility and mica with good flexibility are selected as the ferromagnetic and flexible layers, respectively. The epitaxial γ'-Fe_4N(00 L) films were directly grown on mica(00 L) substrates by facing-target reactive sputtering. The magnetic and electronic transport properties in flexible γ'-Fe_4N/mica films were investigated systematically at the bending or released states. It is found that the M_s, magnetic anisotropy, longitudinal resistance, and anomalous Hall resistivity of the γ'-Fe_4N film can be effectively tailored by the bending-induced strains. At a tensile strain with a radius of curvature (ROC) of 3 mm, the M_s change can reach up to 210%. At a tensile strain of ROC = 2 mm, the out-of-plane M_r/M_s is six times larger than that of unbent γ'-Fe_4N films. Moreover, the longitudinal resistance R_{xx} and anomalous Hall resistivity ρ_{xy} were tunable by different tensile or compressive strains, where the strain-tailored multiresistance states appear. The large strain-tailored magnetic and electronic transport properties can be mainly attributed to the shift of the nitrogen position at different bending strains besides the magneto-/electromechanical coupling and misorientation effects. The flexible epitaxial γ'-Fe_4N films have the potential applications in the magneto-/electromechanical wearable devices with the strain tunable characteristics.

■ EXPERIMENTAL DETAILS

Sample Preparation. Based on the layered mica substrates stacked by van der Waals forces, the mica substrates were cleaved to obtain a smooth and clean surface before depositing the γ'-Fe_4N films. The mica substrate was placed and fixed on a clean and flat weighing paper. Meanwhile, a sharp surgical blade-assisted sharp tweezer was used to lightly cleave the substrate. Finally, a fresh and smooth surface can be obtained in the separated mica. Epitaxial γ'-Fe_4N films with different thicknesses (t = 3, 6, 18, 30, and 48 nm) were directly deposited on the mica substrate at 450 °C by a DC reactive facing-target sputtering from a pair of Fe targets (99.95%). The Ar (99.999%) and N_2 (99.999%) gas mixture was introduced into the chamber with a mixing ratio of Ar:N_2 = 5:1, where the sputtering pressure was 1.0 Pa. The sputtering power on the targets was 37.5 W. The deposition rate was 2.1 nm/min.[31,45] The film thickness was measured by a Dektak 6 M surface profiler and calibrated by transmission electron microscopy (TEM).

Structure Analysis. The surface morphology was analyzed by Bruker MultiMode 8 atomic force microscopy (AFM). Meanwhile, the magnetic domain was characterized by magnetic force microscopy (MFM). The microstructures of the films was observed by X-ray diffraction (XRD) with Cu Kα radiation (λ = 1.5406 Å), high resolution synchrotron X-ray diffraction (SXRD) with beamline 1W1A and λ = 1.5491 Å, and high resolution transmission electron microscopy (HRTEM). Meanwhile, the quantitative map (Qmap) was obtained. The atomic resolution scanning transmission electron microscopy (STEM) analyses in the high-angle annular dark field (STEM-HAADF) mode were also conducted to investigate the microstructure of γ'-Fe_4N/mica films by an aberration-corrected Titan Themis G2 microscope at 300 kV with a beam current of 50 pA. TEM samples were prepared using a focused ion beam (FIB) followed by FEI STRATA DB235.

Magnetic Characterization. The magnetic properties of γ'-Fe_4N/mica films at tensile or compressive strains of different ROCs were measured by a Quantum Design magnetic properties measurement system. The magnetic field was along the γ'-Fe_4N [100] or [001] direction. Meanwhile, the bending strain of γ'-Fe_4N films was along the γ'-Fe_4N [010] direction. A series of molds with the ROCs of 2, 3, and 5 mm were used to apply the tensile or compressive strain by attaching a γ'-Fe_4N/mica film on the molds. Especially, to ensure the accuracy of the measured data, the tests of the tensile or compressive strain were conducted on the same sample, where the compressive strain tests were processed right after the tensile strain tests.

Electronic Transport Property Characterization. The electronic transport properties of γ'-Fe_4N/mica films with different ROCs were conducted by a Quantum Design physical property measurement system. The epitaxial γ'-Fe_4N/mica films with the five-terminal Hall bar were prepared to measure the temperature- and magnetic field-dependent transverse resistivity $\rho_{xx}(T)$ and $\rho_{xx}(H)$ (namely, MR), anomalous Hall resistivity $\rho_{xy}(H)$, anisotropy magnetoresistance (AMR), and planar Hall resistivity (PHR) at different tensile or compressive strains. The real $\rho_{xy}(H)$ was obtained by $\rho_{xy}(H) = \frac{\rho_{xy}(+H) - \rho_{xy}(-H)}{2}$, where $\rho_{xy}(+H)$ and $\rho_{xy}(-H)$ are the Hall resistivities at the positive and negative magnetic field at the same values, respectively.

First Principles Calculations. The first principles calculations were performed in a Vienna Ab initio Simulation Package based on the projector-augmented wave method.[46,47] The generalized gradient approximation (GGA) of the Perdew-Burke-Ernzerhof (PBE) form was used for the exchange correlation function.[48] The energy cutoff for the plane-wave basis set was 500 eV. The convergence criteria of the energy and atomic forces were, respectively, set to 10^{-5} eV and 0.01 eV $Å^{-1}$. The Brillouin zone is sampled with a Γ-centered 9 × 9 × 9 k-mesh for bulk γ'-Fe_4N. Based on the magnetic force theorem, the magnetic anisotropy energy (MAE) was calculated by considering spin-orbit-coupling (SOC),[49,50] where the charge density was read for both the in- and out-of-plane magnetization orientations. In order to obtain orbital resolved-MAE, the MAE on the orbital λ of the atom i was determined by $MAE_{i\lambda} = \frac{E_{i\lambda}^{out} - E_{i\lambda}^{in}}{a \times b \times c}$, where a, b, and c are the lattice constants of the strained γ'-Fe_4N. A positive or negative value of MAE represented the IMA or PMA, respectively. The total MAE was obtained by calculating the sum of MAE_i for all atoms, where the MAE_i of the single atom i was calculated by $MAE_i = \sum_\lambda MAE_{i\lambda}$of all orbitals.

■ RESULTS AND DISCUSSION

The schematic diagrams of bending configurations to produce the tensile or compressive strains in the magnetic and

https://dx.doi.org/10.1021/acsami.0c08042
ACS Appl. Mater. Interfaces 2020, 12, 27394−27404

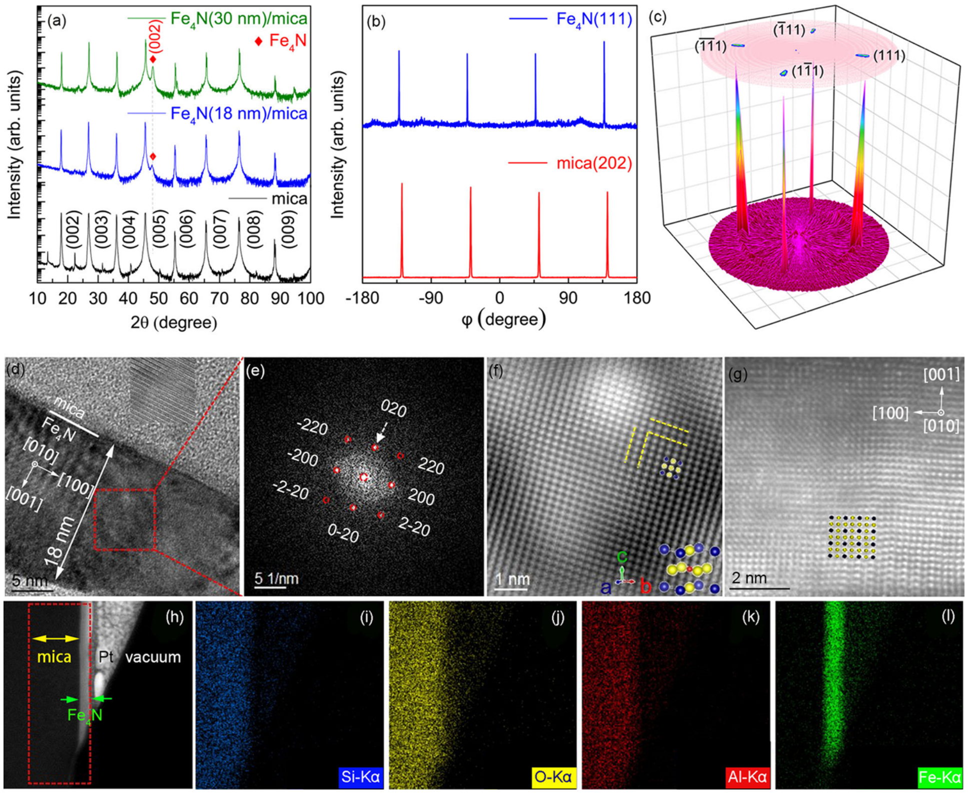

Figure 1. Microstructure characterizations of γ'-Fe_4N/mica: (a) XRD $\theta-2\theta$ patterns, (b) XRD φ-scans, (c) XRD pole figure. (d) Cross-sectional HRTEM, (e) fast Fourier transform image of the red areas in (d), (f) inverse fast Fourier transform pattern of (e), (g) HAADF-STEM image of the γ'-Fe_4N layer. (h) HAADF-STEM image the whole sample, (i–l) EDS elemental mappings of (i) Si, (j) O, (k) Al, and (l) Fe corresponding to (h).

electronic transport measurements are shown in Figure S1a–h of the Supporting Information. As shown in Figure S1a,c, when the γ'-Fe_4N film is located above the mica with an outward bending direction, the tensile strain will be generated along the γ'-Fe_4N [010] direction. In contrast, as the γ'-Fe_4N film sits under the mica with an inward bending direction (Figure S1b,d in the Supporting Information), a compressive strain along the γ'-Fe_4N [010] direction can be induced. A series of molds with ROC = 2, 3, and 5 mm were used to apply different tensile or compressive strains by attaching the γ'-Fe_4N/mica films on the molds. In the text, ∞, +2 mm, +3 mm, +5 mm, +∞, −2 mm, −3 mm, −5 mm, and −∞ represent the unbent, tensile strain of ROC = 2 mm, tensile strain of ROC = 3 mm, tensile strain of ROC = 5 mm, tensile released, compressive strain of ROC = 2 mm, compressive strain of ROC = 3 mm, compressive strain of ROC = 5 mm, and compressive released. In order to briefly describe the four states by considering the magnetic field and the bending strain direction, the states are labeled as "IP-Tensile", "OP-Tensile", "IP-Compressive", and "OP-Compressive", which represent the cases with the in-plane magnetic field along the γ'-Fe_4N [100] direction at a tensile strain, the out-of-plane magnetic field along the γ'-Fe_4N [001] direction at a tensile strain, the in-plane magnetic field along the Fe_4N [100] direction at a compressive strain, and the out-of-plane magnetic field along the γ'-Fe_4N [001] direction at a compressive strain, respectively. Figure S2a shows the morphology of the cleaved surface on the separated mica by atomic force microscopy (AFM). The root-mean-square surface roughness R_q of the cleaved mica is only 0.05 nm, which is an order of magnitude smaller than 0.18 nm as obtained by Liu et al.[16] This result confirms that an extremely clean and smooth surface of the mica substrate has been obtained, which is helpful to deposit the high-quality epitaxial films. In order to observe the quality of the film bent 50 times at a tensile or compressive strain of ROC = 2 mm, the AFM images of the bent films are shown in Figure S2c,d. One can see that R_q increases from 0.73 nm for the unbent γ'-Fe_4N(18 nm)/mica to 0.84 nm for the tensile-released one, then decreases to 0.64 nm for the compressive-released one. The small R_q fluctuation indicates that the γ'-Fe_4N film keeps well after applying the tensile or compressive strains. Meanwhile, Figure S2e–i shows the schematic diagrams of γ'-Fe_4N films with 4 × 6 mm^2 size at five tensile states, which further suggests the good flexibility of γ'-Fe_4N films. In addition, the surface morphography of γ'-Fe_4N/mica films with different thicknesses shows the smooth surface of the films, as shown in Figure S3 of the Supporting Information.

Figure 1a shows the X-ray diffraction (XRD) $\theta-2\theta$ patterns of the mica and γ'-Fe_4N/mica films. Only the mica(00 L) and γ'-Fe_4N(002) diffraction peaks can be detected, which suggests the prefered orientation of γ'-Fe_4N films. Based on Bragg's law, the calculated lattice constant of the γ'-Fe_4N film is 3.799 ± 0.006 Å, which is in well agreement with 3.795 Å of bulk γ'-Fe_4N (JCPDS card No. 06-0627). Moreover, XRD φ-scans of γ'-Fe_4N(111) and mica(202) peaks at 90° intervals are shown in Figure 1b, where 2θ and α were fixed at 41.22 and 35.26° for the γ'-Fe_4N(111) peak and 42.84 and 54.13° for the mica(202) peak, respectively. The φ-scan results reveal that γ'-Fe_4N films with an in-plane fourfold symmetry may epitaxially grow on mica substrates. In order to further confirm the epitaxial growth of γ'-Fe_4N films on mica, Figure 1c shows the XRD pole figure of the γ'-Fe_4N(111) peak, where the periodic

https://dx.doi.org/10.1021/acsami.0c08042
ACS Appl. Mater. Interfaces 2020, 12, 27394–27404

intensity variation of the cubic lattice can be observed in the γ'-Fe_4N film. The XRD pole figure confirms the epitaxial relationship between the γ'-Fe_4N film and the mica substrate as $[001]_{Fe4N}//[001]_{mica}$.

It can be noted that the lattice mismatch is as high as ~27% between γ'-$Fe_4N[100]$ and mica[100], where the lattice constants of γ'-Fe_4N (cubic) are $a = b = c = 3.795$ Å, $\alpha = \beta = \gamma = 90°$ and those of mica (monoclinic) are $a = 5.208$ Å, $b = 8.995$ Å, $c = 10.275$ Å, $\alpha = 90°$, $\beta = 101.6°$, $\gamma = 90°$. Generally, the large lattice mismatch will lead to the formation of a rough interface caused by a number of misfit dislocations. However, a sharp and clear interface between γ'-Fe_4N and mica can be observed from the cross-sectional high resolution transmission electron microscopy (HRTEM) image, as shown in Figure 1d. Meanwhile, the cross-sectional TEM image and the selected area electron diffraction (SAED) pattern of mica(001) are shown in Figure S4 of the Supporting Information, which suggests a layer structure of mica. Figure 1e,f displays the fast Fourier transform and inverse fast Fourier transform patterns from the red square region shown in Figure 1d. As shown in Figure 1e,f, one can clearly see the diffraction spots from γ'-Fe_4N and the orderly arranged Fe_I (blue dots) and Fe_{II} (yellow dots) atoms of the γ'-Fe_4N layer. Additionally, Figure 1g shows the cross-sectional STEM-HAADF image of γ'-Fe_4N lattices. Some distortions appear in the face-centered cubic γ'-Fe_4N [001] lattice on the mica [001] substrate, which is tightly related to the flexible strains from the mica substrate. As shown in Figure 1g, no intermixing or defects appear, which further confirms the epitaxial growth of γ'-Fe_4N by the fast Fourier transform and XRD pole figure. Therefore, the γ'-Fe_4N film can be epitaxially grown on flexible mica even though a large lattice mismatch exists, which should be attributed to the misfit dislocation.[31,51] Misfit dislocation is the distortion of the lattice of the γ'-Fe_4N films near the interface, which can release the large strain induced by the lattice of the substrate. Normally, the misfit dislocation appears in the heterogeneous systems with a large lattice mismatch between the film and the substrate, such as a −9.92% lattice mismatch of γ'-Fe_4N/MgO.[31] Furthermore, the Qmaps of Si, O, Al, and Fe elements from the mica substrate and γ'-Fe_4N films can be observed in Figure 1i−l, which are selected by a red box as shown in Figure 1h. It is clear that the Fe elements are uniformly distributed in the γ'-Fe_4N layer. The uniform distribution of each element also suggests that the γ'-Fe_4N/mica has a sharp interface without the serious interdiffusion.

First, the magnetic force microscopy (MFM) images of unbent γ'-Fe_4N/mica films with different thicknesses have been measured, which shows a good ferromagnetic state (Figure S5 of the Supporting Information). Next, the room-temperature in-plane and out-of-plane $M-H$ curves of γ'-Fe_4N/mica films with different thicknesses were measured at different tensile or compressive strains. Figure 2a shows the in-plane $M-H$ curves of the 3 nm-thick γ'-Fe_4N film at a tensile strain. It is found that M_s increases and H_c decreases as ROC decreases from unbent to ROC = 3 mm. At ROC<3 mm, M_s decreases and H_c increases. Moreover, as the tensile strain increases, M_s and H_c gradually recover, but are slightly lower than the initial unbent state, which indicate the excellent ductility and flexibility of γ'-Fe_4N films. The in-plane $M-H$ curves of γ'-Fe_4N films with thicknesses of 6, 18, 30, and 48 nm are also measured at different tensile strains, as shown in Figure 2b−e. At different film thicknesses, the M_s and H_c of γ'-Fe_4N films show a similar strain-dependent behavior to that of

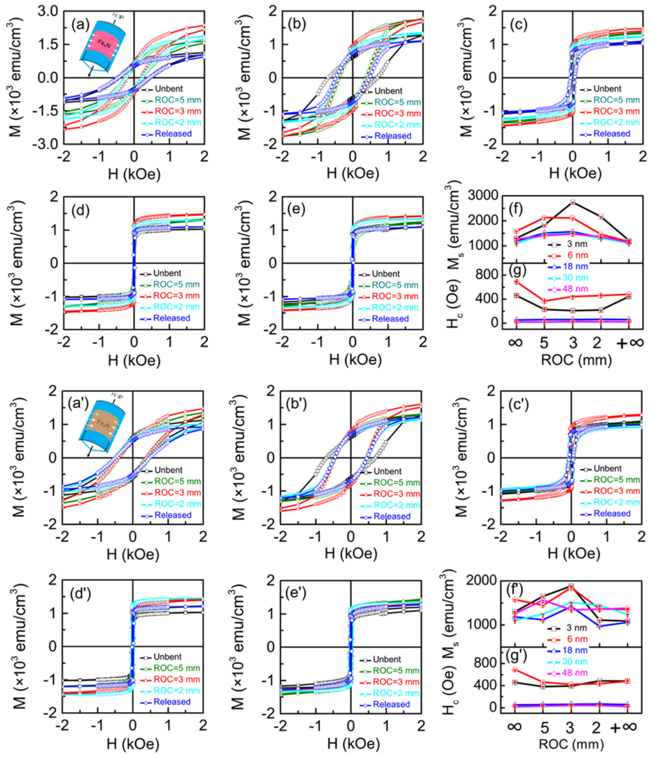

Figure 2. In-plane $M-H$ loops of γ'-Fe_4N films with the different thicknesses at (a−g) tensile and (a′−g′) compressive strains at 300 K: (a, a′) 3 nm, (b, b′) 6 nm, (c, c′) 18 nm, (d, d′) 30 nm, and (e, e′) 48 nm Fe_4N film. The dependence of (f, f′) saturation magnetization and (g, g′) coercivity of γ'-Fe_4N films with different thicknesses at different (f−g) tensile or (f′−g′) compressive strains.

the 3 nm-thick one, as shown in Figure 2f,g. It is found that the smaller the film thickness is, the larger the tunability of magnetic properties in flexible epitaxial γ'-Fe_4N/mica films, which suggests that a thinner γ'-Fe_4N film is more sensitive to the bending strain. Meanwhile, in the thickness-dependent magnetization of γ'-Fe_4N films at different bending strains, one can find that the M_s in a thinner γ'-Fe_4N film is larger, especially at a tensile or compressive strain of ROC = 3 mm. The larger M_s in a thinner film (like the 3 nm-thick γ'-Fe_4N film) may be associated with the formation of a magnetic FeN-dominant phase with a large magnetization.[52−54] As shown in Figure 2f,g, the maximum M_s and minimum H_c of the γ'-Fe_4N film with different thicknesses appear at a tensile strain of ROC = 3 mm. Moreover, the in-plane $M-H$ curves of the γ'-Fe_4N film with different thicknesses at a compressive strain are shown in Figure 2a′−g′. The M_s and H_c change trend of γ'-Fe_4N films at the compressive strain is similar to that at the tensile strains. Additionally, the out-of-plane M_s and H_c of γ'-Fe_4N films with different thicknesses at the tensile or compressive strains are shown in Figure S6 of the Supporting Information. The strain-dependent out-of-plane M_s and H_c shows the same tendency with the in-plane cases at the tensile or compressive strains. Therefore, in γ'-Fe_4N/mica films, the tensile strain influence on the in-plane or out-of-plane M_s and H_c is the same as that of the compressive strain. Namely, the change trend of M_s and H_c is similar at IP-tensile, OP-tensile, IP-compressive, and OP-compressive states. It is noted that the magnetic response of γ'-Fe_4N films to bending strain is distinguished with that of other ferromagnetic materials. For example, in $CoFe_2O_4$, $Fe_{81}Ga_{19}$, and $Co_{40}Fe_{40}B_{20}$ films, the

https://dx.doi.org/10.1021/acsami.0c08042
ACS Appl. Mater. Interfaces 2020, 12, 27394−27404

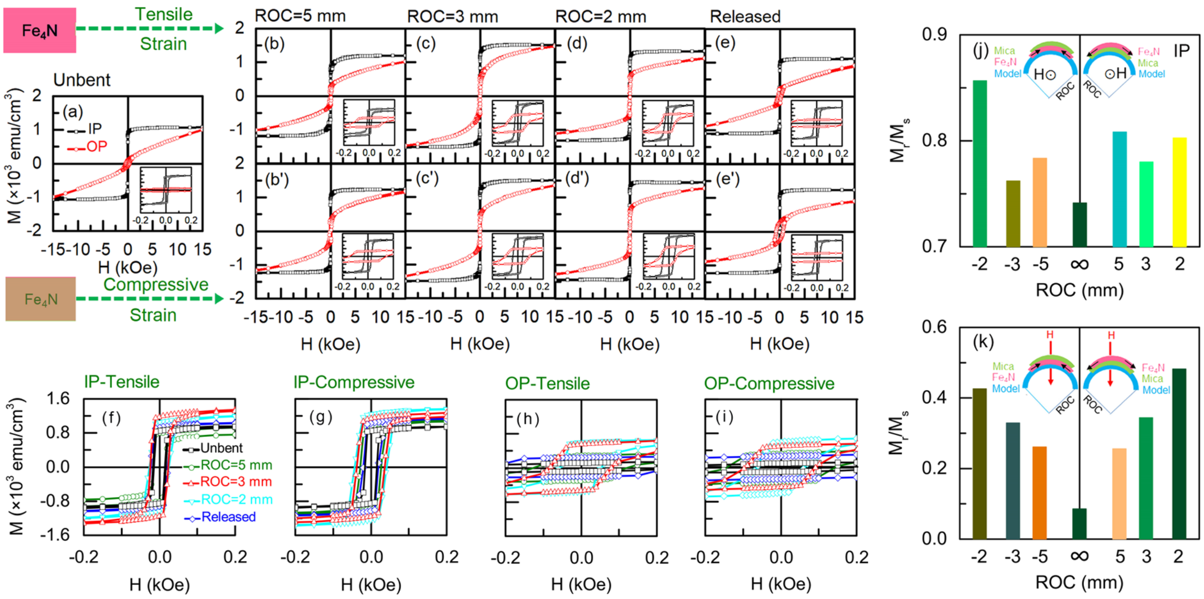

Figure 3. $M-H$ loops of the γ'-Fe_4N(30 nm) film at (a) unbent, (b−e) tensile strains at different radius of curvatures (ROCs), (b′−e′) compressive strains at different ROCs. (f) $M-H$ loops with the in-plane magnetic field at tensile strains, (g) $M-H$ loops with the in-plane magnetic field at compressive strains, (h) $M-H$ loops with the out-of-plane magnetic field at tensile strains and (i) $M-H$ loops with the out-of-plane magnetic field at compressive strains. (j) In-plane and (k) out-of-plane M_r/M_s at different strain ROCs.

tensile strain effect on magnetic properties is opposite to that of compressive strains.[14,26,55] Meanwhile, the bending strain influence on magnetic properties has been ascribed to the magnetomechanical coupling effect, which is tightly associated with a large magnetostrictive coefficient, such as −590 ppm in $CoFe_2O_4$ films and 350 ppm in $Fe_{81}Ga_{19}$ films.[26,55] However, the M_s change trend of γ'-Fe_4N/mica films at different tensile or compressive strains cannot be explained by the magnetostrictive effect even though a magnetostrictive coefficient of −143 ppm exists in γ'-Fe_4N.[56,57] Therefore, the strain-tailored magnetic properties of γ'-Fe_4N/mica films may be associated with other factors induced by the magnetomechanical coupling effect.

The diagram in Figure S7 shows the M_s(ROC*s*)/M_s(Unbent) and H_c(ROC*s*)/H_c(Unbent) of γ'-Fe_4N films with different thicknesses at 300 K. As shown in Figure S7a−d, a peak of M_s(ROC*s*)/M_s(Unbent) curves appears at ROC = 3 mm, where the M_s(ROC*s*)/M_s(Unbent) is in the range from 1.17 to 2.10 at the IP-tensile state, 0.97 to 2.07 at the OP-tensile state, 1.06 to 1.45 at the IP-compressive state, and 1.08 to 1.41 at the OP-compressive state. The M_s change of γ'-Fe_4N films can reach up to 210%. The largest value in the reported ferromagnetic/mica systems is 267% (from 1.2 to 3.2 μ_B per Ru) in $SrRuO_3$/mica films at 10 K, which cannot be used in the devices at room temperature.[37] In $CoFe_2O_4$ films, M_s change is less than 150% (from 100 to 150 emu/cm^3).[55] In $La_{0.67}Sr_{0.33}MnO_3$ films, no significant change of M_s was observed at both the tensile and compressive strains.[15] Therefore, the large strain-tailored M_s of γ'-Fe_4N/mica films at room temperature is of great significance for the practical applications in flexible spintronic devices. Figure S7e−h shows the H_c(ROCs)/H_c(Unbent) of γ'-Fe_4N films with different thicknesses, which shows the opposite trend with M_s(ROCs)/M_s(Unbent). In a ferromagnetic film, the M_s and H_c will satisfy the relation of

$$\frac{pk_{\text{eff}}}{\mu_0} = M_s \times H_c \tag{1}$$

where k_{eff} is the effective anisotropy constant, p is a dimensionless factor that depends on the type of magnetic anisotropy, and μ_0 is the permeability in vacuum.[58,59] Reasonably, an inverse relationship exists between M_s and H_c. Based on eq 1, $k'_{\text{eff}}/k_{\text{eff}}$ can be obtained by calculating $(M'_s \times H'_c)/(M_s \times H_c)$, where M'_s (M_s) and H'_c (H_c) are obtained under a bent (unbent) state, as shown in Figure S8. Moreover, $k'_{\text{eff}}/k_{\text{eff}}>1$ (or <1) means that k_{eff} increases (or decreases) by applying a strain. In 30 nm-thick γ'-Fe_4N films, a peak of the in-plane $k'_{\text{eff}}/k_{\text{eff}}$ can be observed at a tensile or compressive strain, as shown in Figure S8a,b. Meanwhile, as shown in Figure S8c,d, a valley of the out-of-plane $k'_{\text{eff}}/k_{\text{eff}}$ appears in the 30 nm-thick γ'-Fe_4N films in spite of a mixture of $k'_{\text{eff}}/k_{\text{eff}}>1$ and $k'_{\text{eff}}/k_{\text{eff}}<1$. It implies that a larger magnetic anisotropy will occur at a certain strain in 30 nm-thick γ'-Fe_4N films.

In order to clarify the mechanism of the strain-tailored magnetic anisotropy of the γ'-Fe_4N film, Figure 3 shows the in-plane and out-of-plane $M-H$ curves of the 30 nm-thick γ'-Fe_4N film at different tensile or compressive strains. For a comparison of strain-tailored magnetic anisotropy, the in-plane and out-of-plane $M-H$ curves of the 3 nm-thick γ'-Fe_4N film at different tensile or compressive strains are shown in Figure S9 of the Supporting Information. The comparison reveals a more significant strain-tailored magnetic anisotropy in the 30 nm-thick γ'-Fe_4N film. As shown in Figure 3a, the in-plane and out-of-plane $M-H$ curves of unbent γ'-Fe_4N films are analyzed first. The in-plane $M-H$ curve is relatively square with a M_r/M_s of 0.74, while the out-of-plane M_r/M_s is only 0.08, which indicates that an in-plane magnetic anisotropy (IMA) exists in the unbent γ'-Fe_4N film. As shown in Figure 3b−d and b′−d′, the in-plane M_r/M_s of the γ'-Fe_4N films is almost a constant of 0.80 ± 0.05 at different tensile or compressive states, which implies that the in-plane M_r/M_s is insensitive to the bending strains. However, the out-of-plane M_r/M_s increases from 0.08

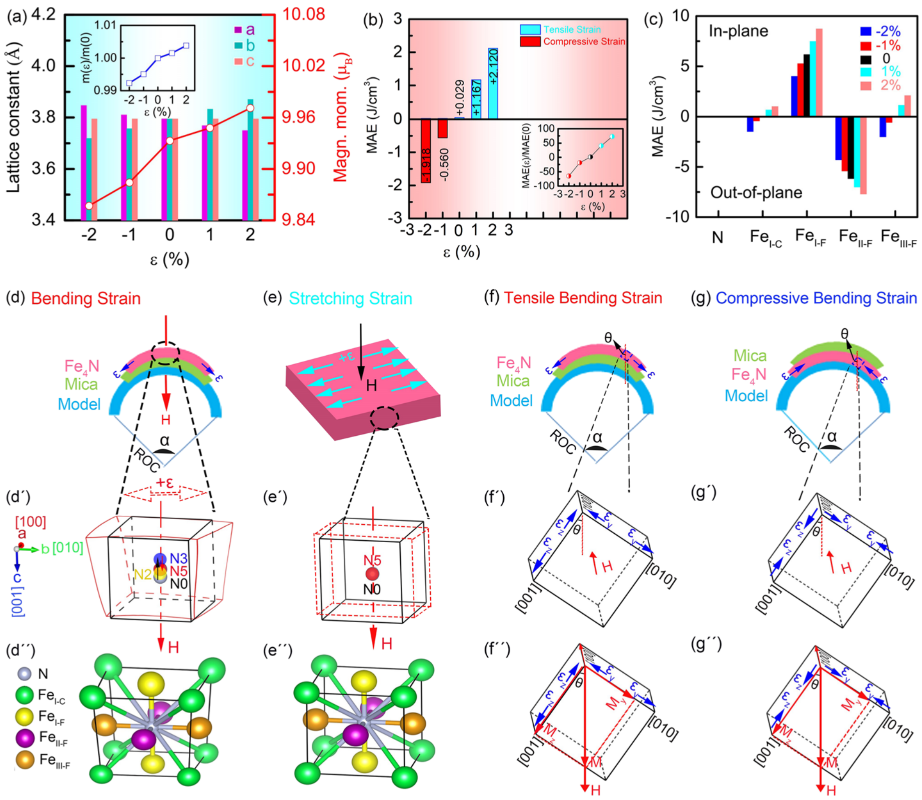

Figure 4. Calculation results using the first principles calculations, (a) lattice constants and magnetic moments of γ'-Fe_4N at different strains, (b) total magnetic anisotropy energy (MAE) of γ'-Fe_4N, (c) single atom MAE at −2%, −1%, unstrained, +1%, and + 2% strain. Schematic diagrams of the mechanism in flexible epitaxial γ'-Fe_4N/mica films at (d−d″) bending strain, (e−e′′) stretching strain, (f−f′′) tensile-bending strain, and (g−g′′) compressive-bending strain.

at the unbent state (ROC = ∞) to 0.25 at a tensile strain of ROC = 5 mm and 0.26 at a compressive strain of ROC = 5 mm, 0.34 at a tensile strain of ROC = 3 mm and 0.33 at a compressive strain of ROC = 3 mm, and 0.48 at a tensile strain of ROC = 2 mm and 0.42 at a compressive strain of ROC = 2 mm, where the out-of-plane M_r/M_s magnitude at tensile or compressive strain is 4.25−6 times larger than that of the unbent γ'-Fe_4N film. In previously reported results, the M_r/M_s change by the bending strains was less than 62% in $Co_{40}Fe_{40}B_{20}$ films and 198% in $CoFe_2O_4$ nanopillar arrays.[7,14] Therefore, the large variation of M_r/M_s in the γ'-Fe_4N film is of great significance for practical applications. As shown in Figure 3e,e′, as the tensile or compressive strain is released, the magnetization gradually recovers to the initial state, which can be seen in the above M_s results. Figure 3f−i shows the M−H curves of the 30 nm-thick γ'-Fe_4N film at IP-tensile, IP-compressive, OP-tensile, and OP-compressive states, where the out-of-plane magnetization can be tailored more significantly than the in-plane one at different tensile or compressive strains. Additionally, the dependences of the in-plane and out-of-plane M_r/M_s on ROC are shown in Figure 3j,k. At either tensile or compressive strain, the M_r/M_s of γ'-Fe_4N film increases with the increase (decrease) of strain (ROC). Meanwhile, the out-of-plane M_r/M_s (Figure 3k) is more sensitive to the strain than the in-plane one (Figure 3j) because the magnitude of the out-of-plane strain-tailored M_r/M_s (425−600%) is much larger than that of the in-plane strain-tailored M_r/M_s (almost a constant).

Based on the magnetic properties of flexible epitaxial γ'-Fe_4N/mica films, it can be demonstrated that the noticeable tunability of M_s and magnetic anisotropy can be induced at a certain bending strain. The strain effects can be derive from the magnetomechanical coupling effect. The ordinary magneto-mechanical coupling effect refers to a 'breathing' distortion of the N_6 octahedron around a given Fe atom.[55,60,61] Here, the bending distortion means that both the proximate 'breathing' distortion and the shift of the nitrogen position in the unit cell appear in the γ'-Fe_4N unit cell due to bending deformation. Note the difference between the 'breathing' distortion and bending distortion; the first principle calculations were performed to illustrate the effect of 'breathing' distortion on the magnetic moments and magnetic anisotropy energy (MAE), as shown in Figure 4a−c. The magnitude of bending strains in experiments can be expressed as $\varepsilon = (t_{Fe4N} + t_{mica})/$ROC, where t_{Fe4N} and t_{mica} are the thickness of the Fe_4N films and mica substrates, respectively.[62] At $t_{Fe4N} \ll t_{mica}$, t_{Fe4N} is negligible. The thickness of mica used in the magnetic measurement is 37.5 μm. Therefore, the five strain states ε can be recorded as ∞, 0.75%, 1.25%, 1.88%, and ± ∞, which corresponds to the unbent, ROC = 5, 3, 2 mm, and released states. Meanwhile, ε or ROC is positive (negative) at the tensile (compressive) strain. Based on the strains (−1.88, −1.25, −0.75, 0, +0.75, +1.25, and +1.88%) in experiments, a strain magnitude of −2%, −1%, 0, +1%, and +2% was used in calculations to manifest the effect of stretching strains (namely, 'breathing' strains) on the magnetic moments and magnetic anisotropy of γ'-Fe_4N films. Here, the stretching strain is referred to the 'breathing' strains caused by 'breathing' distortion. In calculations, the magnitude of in-plane uniaxial strain ε is defined as $(b-b_0)/b_0 \times 100\%$, where b and b_0 (b_0 =

https://dx.doi.org/10.1021/acsami.0c08042
ACS Appl. Mater. Interfaces 2020, 12, 27394−27404

3.795 Å) are the lattice constants of the strained and unstrained γ'-Fe_4N. Meanwhile, the in-plane uniaxial strain is applied along the b-axis direction (namely, the γ'-Fe_4N [010] direction). The in-plane (out-of-plane) magnetic field is along the a-axis (c-axis) direction, namely, the γ'-Fe_4N [100] (γ'-Fe_4N [001]) direction. As shown in Figure 4a, the magnetic moments of γ'-Fe_4N increase from 9.933 to 9.971 μ_B, as the tensile strain increases from 0 to +2%. Meanwhile, as the compressive strain changes from 0 to −2%, the magnetic moments of γ'-Fe_4N decrease from 9.933 to 9.857 μ_B. Therefore, the magnetic moments of γ'-Fe_4N increases (decreases) with the increase of tensile (compressive) strain, which is similar to the M_s change of $CoFe_2O_4$ films.[55] Meanwhile, M_s change has been ascribed to the proximate 'breathing' distortion caused by the bending strain.[7,55] Specifically, the magnetic moment change ($m(\varepsilon)/m(0)$) is only 99.23−100.38% at stretching strains of $\varepsilon = \pm 2\%$ (see the inset of Figure 4a), which is much smaller than the M_s change (141−210% at ROC = ±3 mm) at the bending strain in experiments. The magnetic moment results in calculations further reveal that other factors like the shift of nitrogen position in the γ'-Fe_4N unit cell caused by the bending strain should be considered besides the proximate 'breathing' distortion, due to the role of the N position in the γ'-Fe_4N unit cell.[63−66]

Figure 4d−d″ and e−e′′ shows the schematic diagrams of the bending distortion caused by bending strains in experiments and 'breathing' distortion induced by stretching strain in calculations, respectively. In order to explain the bending strain-tailored M_s of γ'-Fe_4N films, a simplified model is established, as shown in Figure 4d−d″. Figure 4d′shows that the position of the nitrogen atom is labeled as position "N0", "N5", "N3", and "N2", which represents the distortion of the γ'-Fe_4N unit cell at tensile strain of ROC = ∞, +5, +3, and +2 mm, respectively. First, in γ'-Fe_4N/mica films, M_s increases as the ROC decreases from ∞ to 3 mm (see Figure 2f and f′), where the nitrogen atom shifts from the N0 to N3 position, as shown in Figure 4d′. Moreover, the sudden change of M_s at a tensile or compressive strain of ROC = 3 mm suggests that the maximum of M_s will appear in the process of ROC from 3 to 2 mm, corresponding to the shift of the nitrogen atom from the N3 to N2 position, as shown in Figure 4d′. Besides, the M_s at tensile strain of ROC = 2 mm is slightly smaller than that at a tensile strain of ROC = 5 mm, as shown in Figure 2f,f′. In the bending γ'-Fe_4N film, the film length L along the bending direction is a constant, where the corresponding central angle of the bending film can be labeled as β. Thus, β will satisfy the dependence of $\beta = L/\mathrm{ROC}$, where β at ROC = 5, 3, and 2 mm is corresponding to 57.29, 95.48, and 143.22°, respectively. Normally, in body-centered cubic, as β increases, the atom located at the body-centered position N0 will move from N0 to N5, N3, and N2. M_s can be considered as an N-shift-related function at different ROCs. Based on all the experimental results of ROC-dependent M_s shown in Figure S7a−d, a sinβ-related function, i.e., $M_s \propto \sin\beta$, may be considered as the functions of M_s and the position of the nitrogen atom under different ROCs. The critical β_0 makes the nitrogen atom shift to position N3, which induces a maximum of M_s. At $\beta < \beta_0$ (namely, ROC > 3 mm), the nitrogen position moves from the N0 to N3 position. Meanwhile, at $\beta > \beta_0$ (namely, ROC < 3 mm), the nitrogen position moves from N3 to N2 position. Reasonably, the similar magnetic behavior at tensile- and compressive-bending strains also can be explained due to the similar shift of the nitrogen position at two bending states. Further, the large shift of the nitrogen position will result in the decrement of nitrogen contribution to the γ'-Fe_4N unit cell, which may form a new phase like α''-$Fe_{16}N_2$. Therefore, the large M_s change of 210% in the bending γ'-Fe_4N should be tightly associated with the large shift of the nitrogen position. In the early 1970s, Kim and Takahashi reported that α''-$Fe_{16}N_2$ has a high M_s of 2320 emu/cm^3.[63] Meanwhile, the crystal structure of α''-$Fe_{16}N_2$ is body-centered tetragonal (bct, a = 5.72 Å, c = 6.29 Å).[64,65] It implies that α''-$Fe_{16}N_2$ can be described as a bct arrangement with an ordered distribution of nitrogen atoms in the deformed octahedral interstices. Interestingly, in the bending γ'-Fe_4N unit cell, both the proximate tetragonal distortion and the shift of nitrogen position appear. Besides, the ferromagnetic structure of γ'-Fe_4N is also of some interest, which is obtained from face-centered cubic γ-Fe with nitrogen placed at the body-center of the unit cell. However, γ-Fe is nonmagnetic.[66] Therefore, the nitrogen position will have a significant influence on the magnetic properties of γ'-Fe_4N. Therefore, the large strain-tailored magnetic properties of γ'-Fe_4N films can be attributed to the proximate tetragonal distortion and the shift of the nitrogen position caused by the bending strains.

In addition, it is also necessary to notice the large enhancement of the out-of-plane squareness. The first principles calculations were conducted to investigate the effect of stretching strain on MAE of γ'-Fe_4N films, as shown in Figure 4b,c. A positive or negative value of MAE represents the IMA or PMA, respectively. Figure 4b shows the total MAE of bulk γ'-Fe_4N at a stretching strain from −2 to +2%. It is found that the total MAE at a tensile (compressive) strain is positive (negative), which means an IMA (PMA). Meanwhile, at a tensile strain of +2%, the total MAE of γ'-Fe_4N is 72.44 times larger than that of the unbent γ'-Fe_4N, as shown in the inset of Figure 4b. At a compressive strain of −1 and −2%, PMA appears, which is different from the above experimental results (see Figure 3). Figure 4c shows the MAE of the single atom at stretching strains from −2 to +2%. The location of each atom in the γ'-Fe_4N unit cell is shown in Figure S10 of the Supporting Information, where the $Fe_{I\text{-}C}$, $Fe_{I\text{-}F}$, $Fe_{II\text{-}F}$, and $Fe_{III\text{-}F}$ represent the Fe atom located at the corner and three face positions of cubic γ'-Fe_4N, respectively. The MAE contribution of N p-orbitals can be negligible. Meanwhile, MAEs of Fe d-orbitals contribute a lot at the tensile or compressive strains. At the tensile strains, the IMA can be mainly attributted to $Fe_{I\text{-}F}$ and $Fe_{III\text{-}F}$ atoms, while the $Fe_{II\text{-}F}$ atom has a great effect on the PMA at the compressive strain. Meanwhile, the d-orbital MAE of $Fe_{I\text{-}C}$ and $Fe_{I\text{-}F}$ and the total density of states (DOSs) of γ'-Fe_4N at a strain of −2%, 0, and + 2% can be observed in Figures S11 and S12 of the Supporting Information, respectively. Previous reports of ferromagnet have confirmed that the tetragonal crystal field can improve magnetic anisotropy.[60,67,68] Therefore, both the enhancement of M_r/M_s in experiments (Figure 3j,k) and the PMA in calculations can be attributed to the tetragonal crystal field, which is resulted from the distortion of Fe_6N octahedron at different bending or stretching strains. Additionally, no PMA appears in experiments, which may be associated with the misorientation effect. As the bending film is applied on an in-plane magnetic field along the γ'-Fe_4N [100] direction, no other magnetic field component appears. However, at an out-of-plane magnetic field, the effective magnetization of the bending film no longer fully contributes to the [001] direction

https://dx.doi.org/10.1021/acsami.0c08042
ACS Appl. Mater. Interfaces 2020, 12, 27394−27404

of the γ'-Fe_4N unit cell due to the misorientation effect caused by the bending films.[69] As shown in Figure 4f″, g″, M is decomposed into the $M_z = M\cos\theta$ and $M_y = M\sin\theta$ components along the γ'-Fe_4N [001] and [010] directions, which results in a larger external magnetic field or energy to satisfy the magnetization saturation. Therefore, in experiments, the enhancement and tunability of magnetic properties originate from the tetragonal distortion and misorientation effect caused by bending strains.

Besides, the effects of bending strain on the electronic transport properties of γ'-Fe_4N/mica films are also investigated, as shown in Figure 5. The schematic diagrams of bending configurations in the electronic transport measurements are shown in Figure S1e−h of the Supporting Information. Figure S13 in the Supporting Information shows the $\rho_{xx}(T)/\rho_{xx}(305\text{ K})$ curves of the γ'-Fe_4N(30 nm)/mica film at different strains. Anomalous Hall resistivity ρ_{xy} and magnetoresistance of γ'-Fe_4N films with different thicknesses of 9−48 nm at 300 K at various bending strains are shown in Figure S14 of the Supporting Information. As shown in Figure S13, ρ_{xx} of the bent γ'-Fe_4N films continuously increases with increasing temperature, which indicates a robust metallic character for the strained γ'-Fe_4N films. Meanwhile, Figure 5a shows the resistance rate defined as $\Delta R = \frac{R_{xx}(\text{ROC}) - R_{xx}(\infty)}{R_{xx}(\infty)} \times 100$, where $R_{xx}(\text{ROC})$ and $R_{xx}(\infty)$, respectively, represent the longitudinal resistance at different ROCs and unbent states. The resistance change of the γ'-Fe_4N film reaches 5% at a tensile strain of ROC = 3 mm. As the tensile strain is released (namely, ROC = +∞), R_{xx} almost retains the resistance states “2”. At a compressive strain of ROC = 3 mm, the R_{xx} change is smaller than that at the tensile-released state. Finally, R_{xx} gradually recovers to the initial state “0” after releasing the compressive strain. Thus, strain-tailored multiresistance states are achieved in the bending γ'-Fe_4N films. Moreover, the strain-tailored anomalous Hall resistivity ρ_{xy} appears where the drop of ρ_{xy} reaches 22% at a tensile strain of ROC = 3 mm, as shown in Figure 5b. It can be found that a ρ_{xy} change of 22% is larger than an R_{xx} change of 5%, which should be ascribed to the weak longitudinal stress and strong transverse stress. Additionally, the magnetoresistance MR of the γ'-Fe_4N(30 nm)/mica film was measured at 300 K at various bending strains, as shown in Figure 5c, where MR is defined as $\text{MR} = \frac{R(H) - R(0)}{R(0)} \times 100$. Compared to ρ_{xy} and MR at the compressive strain, they are more sensitive to the tensile strain.

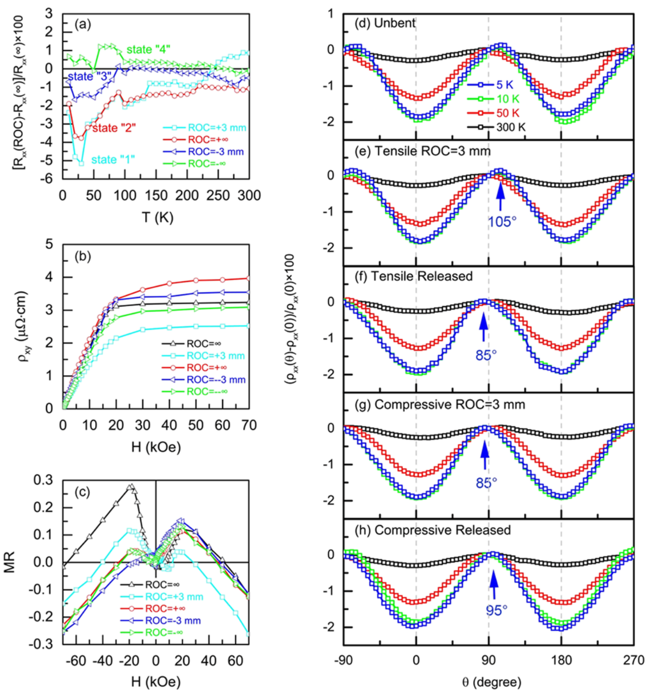

Figure 5. (a) $\frac{R_{xx}(\text{ROC}) - R_{xx}(\infty)}{R_{xx}(\infty)} \times 100$, (b) anomalous Hall resistivity ρ_{xy} curves, and (c) magnetoresistance MR of the γ'-Fe_4N(30 nm)/mica film at different bending strains. (d−h) Anisotropy magnetoresistance AMR of the γ'-Fe_4N(30 nm)/mica film measured at different temperatures of 5−300 K by applying different strains, (d) unbent, (e) tensile strain of ROC = 3 mm, (f) tensile released, (g) compressive strain of ROC = 3 mm, and (h) compressive released states.

Figure 5d−h show the anisotropy magnetoresistance (AMR) of the γ'-Fe_4N(30 nm)/mica film measured at temperatures of 5−300 K by applying different tensile or compressive strains. AMR is defined as $\text{AMR} = \frac{\rho_{xx}(\theta) - \rho_{xx}(0)}{\rho_{xx}(0)} \times 100$. In Figure 5d−h, AMRs at different bending strains show negative values, which should be attributed to the spin-down conduction electrons in γ'-Fe_4N films.[70,71] At 5 K, the AMR phase shifts from 105° at a tensile strain of ROC = 3 mm, to 85° at the tensile-released state, 85° at a compressive strain of ROC = 3 mm, 95° at the compressive released state. AMR of γ'-Fe_4N films is intimately related to the magnetocrystalline anisotropy.[28] Therefore, the shift of the AMR phase indicates that the magnetocrystalline anisotropy of the γ'-Fe_4N film is changed. The shift of the AMR phase at different strains should be associated with the shift of the nitrogen position in the γ'-Fe_4N unit cell induced by the bending film. Therefore, the strain-tailored electronic transport properties can be ascribed to the electromechanical coupling effect induced by the proximate tetragonal distortion and the nitrogen position shift in the bending γ'-Fe_4N unit cell. In previously reported results, the changes of the resistance, ρ_{xy}, MR, AMR, or R_{xy} at the bending strains are not significant in some ferromagnetic/mica systems, such as Fe_3O_4/mica and VO_2/mica,[32,72] which retain the superior performance of the epitaxial counterparts on rigid substrates and enrich the applications in spintronic devices. It can be noted that the electronic transport properties of γ'-Fe_4N/mica films remain well in spite of the bending deformation. Therefore, the flexible epitaxial γ'-Fe_4N films have the potential applications in the electromechanical wearable devices with the strain tunable properties. Meanwhile, the planar Hall resistance R_{xy} of the γ'-Fe_4N(30 nm)/mica film are also measured at various bending strains, as shown in Figure S15 of the Supporting Information.

■ CONCLUSIONS

In summary, the flexible epitaxial γ'-Fe_4N films were directly deposited on mica by reactive facing-target sputtering. Strain-tailored M_s, magnetic anisotropy, and electronic transport properties can be achieved at room temperature by changing the ROCs. M_s of γ'-Fe_4N films at a tensile strain of ROC = 3 mm is significantly tailored with a maximal variation of 210%. Moreover, the out-of-plane M_r/M_s at a tensile strain of ROC = 2 mm is six times larger than that at the unbent state. Meanwhile, the out-of-plane M_r/M_s is more sensitive to the

https://dx.doi.org/10.1021/acsami.0c08042
ACS Appl. Mater. Interfaces 2020, 12, 27394−27404

strains than the in-plane one. In addition, the strain-tailored R_{xx} and ρ_{xy} appear, where the R_{xx} (ρ_{xy}) change reaches 5% (22%) at a tensile strain of ROC = 3 mm. Furthermore, the shift of AMR and PHR phases also appear in the bending γ'-Fe_4N films. This work reports the bending strain manipulation on the M_s, magnetic anisotropy and electronic transport properties of ferromagnetic films effectively. The flexible epitaxial γ'-Fe_4N films have the potential applications in the magneto-/electromechanical wearable spintronic devices.

■ ASSOCIATED CONTENT

Supporting Information

The Supporting Information is available free of charge at https://pubs.acs.org/doi/10.1021/acsami.0c08042.

Details of Schematics of the bending configurations, surface morphographies, TEM image of the mica substrate, magnetic domain, magnetic properties of other thicknesses, magnetic anisotropy, density of states, unit cell of γ'-Fe_4N, and electronic transport property of epitaxial γ'-Fe_4N/mica heterostructures (PDF).

■ AUTHOR INFORMATION

Corresponding Author

Wenbo Mi − *Tianjin Key Laboratory of Low Dimensional Materials Physics and Preparation Technology, School of Science, Tianjin University, Tianjin 300354, China;* orcid.org/0000-0002-9108-9930; Email: miwenbo@tju.edu.cn

Authors

Xiaohui Shi − *Tianjin Key Laboratory of Low Dimensional Materials Physics and Preparation Technology, School of Science, Tianjin University, Tianjin 300354, China*

Mei Wu − *International Center for Quantum Materials, School of Physics, Peking University, Beijing 100871, China*

Zhengxun Lai − *Tianjin Key Laboratory of Low Dimensional Materials Physics and Preparation Technology, School of Science, Tianjin University, Tianjin 300354, China*

Xujing Li − *Electron Microscopy Laboratory, School of Physics, Peking University, Beijing 100871, China*

Peng Gao − *International Center for Quantum Materials, School of Physics and Electron Microscopy Laboratory, School of Physics, Peking University, Beijing 100871, China;* orcid.org/0000-0003-0860-5525

Complete contact information is available at: https://pubs.acs.org/10.1021/acsami.0c08042

Notes

The authors declare no competing financial interest.

■ ACKNOWLEDGMENTS

This work is supported by the National Natural Science Foundation of China (51871161 and 51671142).

■ REFERENCES

(1) Zhang, Y.; Ma, C. R.; Lu, X. L.; Liu, M. Recent Progress on Flexible Inorganic Single-Crystalline Functional Oxide Films for Advanced Electronics. *Mater. Horiz.* **2019**, *6*, 911−930.

(2) Bitla, Y.; Chu, Y. H. MICAtronics: A New Platform for Flexible X-tronics. *FlatChem* **2017**, *3*, 26−42.

(3) Bao, Z. N.; Chen, X. D. Flexible and Stretchable Devices. *Adv. Mater.* **2016**, *28*, 4177−4179.

(4) Karnaushenko, D.; Makarov, D.; Stöber, M.; Karnaushenko, D. D.; Baunack, S.; Schmidt, O. G. High-Performance Magnetic Sensorics for Printable and Flexible Electronics. *Adv. Mater.* **2015**, *27*, 880−885.

(5) Melzer, M.; Kaltenbrunner, M.; Makarov, D.; Karnaushenko, D.; Karnaushenko, D.; Sekitani, T.; Someya, T.; Schmidt, O. G. Imperceptible Magnetoelectronics. *Nat. Commun.* **2015**, *6*, 6080.

(6) Alnassar, M. Y.; Ivanov, Y. P.; Kosel, J. Flexible Magnetoelectric Nanocomposites with Tunable Properties. *Adv. Electron. Mater.* **2016**, *2*, 1600081.

(7) Shen, L. K.; Liu, M.; Ma, C. R.; Lu, L.; Fu, H. R.; You, C. Y.; Lu, X. L.; Jia, C.-L. Enhanced Bending Tuned Magnetic Properties in Epitaxial Cobalt Ferrite Nanopillar Arrays on Flexible Substrates. *Mater. Horiz.* **2018**, *5*, 230−239.

(8) Wang, S.; Xu, J.; Wang, W. C.; Wang, G. N.; Rastak, R.; Molina-Lopez, F.; Chung, J. W.; Niu, S.; Feig, V. R.; Lopez, J.; Lei, T.; Kwon, S. K.; Kim, Y.; Foudeh, A. M.; Ehrlich, A.; Gasperini, A.; Yun, Y. J.; Murmann, B.; Tok, J. B. H.; Bao, Z. N. Skin Electronics from Scalable Fabrication of an Intrinsically Stretchable Transistor Array. *Nature* **2018**, *555*, 83−88.

(9) Gao, W.; Emaminejad, S.; Nyein, H. Y. Y.; Challa, S.; Chen, K.; Peck, A.; Fahad, H. M.; Ota, H.; Shiraki, H.; Kiriya, D.; Lien, D. H.; Brooks, G. A.; Davis, R. W.; Javey, A. Fully Integrated Wearable Sensor Arrays for Multiplexed in Situ Perspiration Analysis. *Nature* **2016**, *529*, 509−514.

(10) Huang, S. Y.; Liu, Y.; Zhao, Y.; Ren, Z. F.; Guo, C. F. Flexible Electronics: Stretchable Electrodes and Their Future. *Adv. Funct. Mater.* **2019**, *29*, 1805924.

(11) Wang, L.; Feng, C.; Li, Y. K.; Meng, F.; Wang, S. R.; Yao, M. K.; Xu, X. L.; Yang, F.; Li, B. H.; Yu, G. H. Switchable Magnetic Anisotropy of Ferromagnets by Dual-Ion-Manipulated Orbital Engineering. *ACS Appl. Mater. Interfaces* **2019**, *11*, 32475−32480.

(12) Xu, Z. D.; Hu, S. B.; Wu, R.; Wang, J. O.; Wu, T.; Chen, L. Strain-Enhanced Charge Transfer and Magnetism at a Manganite/Nickelate Interface. *ACS Appl. Mater. Interfaces* **2018**, *10*, 30803−30810.

(13) Chen, A. T.; Wen, Y.; Fang, B.; Zhao, Y. L.; Zhang, Q.; Chang, Y. S.; Li, P. S.; Wu, H.; Huang, H. L.; Lu, Y. L.; Zeng, Z. M.; Cai, J. W.; Han, X. F.; Wu, T.; Zhang, X. X.; Zhao, Y. G. Giant Nonvolatile Manipulation of Magnetoresistance in Magnetic Tunnel Junctions by Electric Fields via Magnetoelectric Coupling. *Nat. Commun.* **2019**, *10*, 243.

(14) Tang, Z.; Wang, B.; Yang, H.; Xu, X.; Liu, Y.; Sun, D.; Xia, L.; Zhan, Q.; Chen, B.; Tang, M.; Zhou, Y.; Wang, J.; Li, R.-W. Magneto-Mechanical Coupling Effect in Amorphous $Co_{40}Fe_{40}B_{20}$ Films Grown on Flexible Substrates. *Appl. Phys. Lett.* **2014**, *105*, 103504.

(15) Huang, J. J.; Wang, H.; Sun, X.; Zhang, Z. H.; Wang, H. Y. Multifunctional $La_{0.67}Sr_{0.33}MnO_3$ (LSMO) Thin Films Integrated on Mica Substrates toward Flexible Spintronics and Electronics. *ACS Appl. Mater. Interfaces* **2018**, *10*, 42698−42705.

(16) Liu, H. J.; Wang, C. K.; Su, D.; Amrillah, T.; Hsieh, Y. H.; Wu, K. H.; Chen, Y. C.; Juang, J. Y.; Eng, L. M.; Jen, S. U.; Chu, Y. H. Flexible Heteroepitaxy of $CoFe_2O_4$/Muscovite Bimorph with Large Magnetostriction. *ACS Appl. Mater. Interfaces* **2017**, *9*, 7297−7304.

(17) Zhang, Z.; Liu, E.; Zhang, W.; Wong, P. K. J.; Xu, Z.; Hu, F.; Li, X.; Tang, J. X.; Wee, A. T. S.; Xu, F. Mechanical Strain Manipulation of Exchange Bias Field and Spin Dynamics in FeCo/IrMn Multilayers Grown on Flexible Substrates. *ACS Appl. Mater. Interfaces* **2019**, *11*, 8258−8265.

(18) Zeng, Z. H.; Wu, T. T.; Han, D. X.; Ren, Q.; Siqueira, G.; Nyström, G. Ultralight, Flexible, and Biomimetic Nanocellulose/Silver Nanowire Aerogels for Electromagnetic Interference Shielding. *ACS Nano* **2020**, *14*, 2927−2938.

(19) McCreary, A.; Ghosh, R.; Amani, M.; Wang, J.; Duerloo, K.-A. N.; Sharma, A.; Jarvis, K.; Reed, E.-J.; Dongare, A.-M.; Banerjee, S.-K.; Terrones, M.; Namburu, R.-R.; Dubey, M. Effects of Uniaxial and Biaxial Strain on Few-Layered Terrace Structures of MoS_2 Grown by Vapor Transport. *ACS Nano* **2016**, *10*, 3186−3197.

(20) Guillon, O.; Thiebaud, F.; Perreux, D. Tensile Fracture of Soft and Hard PZT. *Int. J. Fract.* **2002**, *117*, 235−246.
(21) Qi, Y.; Kim, J.; Nguyen, T. D.; Lisko, B.; Purohit, P. K.; McAlpine, M. C. Enhanced Piezoelectricity and Stretchability in Energy Harvesting Devices Fabricated from Buckled PZT Ribbons. *Nano Lett.* **2011**, *11*, 1331−1336.
(22) Che, W. R.; Xiao, X. F.; Sun, N. Y.; Zhang, Y. Q.; Shan, R.; Zhu, Z. G. Critical Anomalous Hall Behavior in Pt/Co/Pt Trilayers Grown on Paper with Perpendicular Magnetic Anisotropy. *Appl. Phys. Lett.* **2014**, *104*, 262404.
(23) Mo, Z.; Wu, G. H.; Bao, D. H. Room-Temperature Preparation and Dielectric Properties of Amorphous $Bi_{3.95}Er_{0.05}Ti_3O_{12}$ Thin Films on Flexible Polyimide Substrates via Pulsed Laser Deposition Method. *Appl. Surf. Sci.* **2012**, *258*, 5323−5327.
(24) Liu, H. F.; Lei, C. X. Low-Temperature Deposited Titanium-Doped Zinc Oxide Thin Films on the Flexible PET Substrate by DC Magnetron Sputtering. *Vacuum* **2011**, *86*, 483−486.
(25) Bretos, I.; Jiménez, R.; Wu, A.; Kingon, A. I.; Vilarinho, P. M.; Calzada, M. L. Activated Solutions Enabling Low-Temperature Processing of Functional Ferroelectric Oxides for Flexible Electronics. *Adv. Mater.* **2014**, *26*, 1405−1409.
(26) Dai, G. H.; Zhan, Q. F.; Liu, Y. W.; Yang, H. L.; Zhang, X. S.; Chen, B.; Li, R. W. Mechanically Tunable Magnetic Properties of $Fe_{81}Ga_{19}$ Films Grown on Flexible Substrates. *Appl. Phys. Lett.* **2012**, *100*, 122407.
(27) Dai, G. H.; Xing, X. J.; Shen, Y.; Deng, X. H. Stress Tunable Magnetic Stripe Domains in Flexible $Fe_{81}Ga_{19}$ films. *J. Phys. D: Appl. Phys.* **2020**, *53*, No. 055001.
(28) Qiao, X. Y.; Wang, B. M.; Tang, Z. H.; Shen, Y.; Yang, H. L.; Wang, J. L.; Zhan, Q. F.; Mao, S.; Xu, X. H.; Li, R. W. Tuning Magnetic Anisotropy of Amorphous CoFeB Film by Depositing on Convex Flexible Substrates. *AIP Adv.* **2016**, *6*, No. 056106.
(29) Zhang, Y.; Mi, W. B.; Wang, X. C.; Zhang, X. X. Scaling of Anomalous Hall Effects in Facing-Target Reactively Sputtered Fe_4N Films. *Phys. Chem. Chem. Phys.* **2015**, *17*, 15435−15441.
(30) Li, Z. R.; Feng, X. P.; Wang, X. C.; Mi, W. B. Anisotropic Magnetoresistance in Facing-Target Reactively Sputtered Epitaxial γ'-Fe_4N Films. *Mater. Res. Bull.* **2015**, *65*, 175−182.
(31) Lai, Z. X.; Li, Z. R.; Liu, X.; Bai, H. L.; Tian, Y. F.; Mi, W. B. Ferromagnetic Resonance of Facing-Target Sputtered Epitaxial γ'-Fe_4N Films: the Influence of Thickness and Substrates. *J. Phys. D: Appl. Phys.* **2018**, *51*, 245001.
(32) Li, C. I.; Lin, J. C.; Liu, H. J.; Chu, M. W.; Chen, H. W.; Ma, C. H.; Tsai, C. Y.; Huang, H. W.; Lin, H. J.; Liu, H. L.; Chiu, P. W.; Van der Chu, Y. H. Waal Epitaxy of Flexible and Transparent VO_2 Film on Muscovite. *Chem. Mater.* **2016**, *28*, 3914−3919.
(33) Ma, C. H.; Lin, J. C.; Liu, H. J.; Do, T. H.; Zhu, Y. M.; Ha, T. D.; Zhan, Q.; Juang, J. Y.; He, Q.; Arenholz, E.; Chiu, P. W.; Chu, Y. H. Van Der Waals Epitaxy of Functional MoO_2 Film on Mica for Flexible Electronics. *Appl. Phys. Lett.* **2016**, *108*, 253104.
(34) Jiang, J.; Bitla, Y.; Huang, C. W.; Do, T. H.; Liu, H. J.; Hsieh, Y. H.; Ma, C. H.; Jang, C. Y.; Lai, Y. H.; Chiu, P. W.; Wu, W. W.; Chen, Y. C.; Zhou, Y. C.; Chu, Y. H. Flexible Ferroelectric Element Based on Van Der Waals Heteroepitaxy. *Sci. Adv.* **2017**, 3, No. e1700121.
(35) Barlow, S. G.; Manning, D. A. C. Influence of Time and Temperature on Reactions and Transformations of Muscovite mica. *Br. Ceram. Trans.* **2013**, *98*, 122−126.
(36) Zheng, W. C.; Zheng, D. X.; Wang, Y. C.; Jin, C.; Bai, H. L. Uniaxial Strain Tuning of the Verwey Transition in Flexible Fe_3O_4/Muscovite Epitaxial Heterostructures. *Appl. Phys. Lett.* **2018**, *113*, 142403.
(37) Liu, J. D.; Feng, Y.; Tang, R. J.; Zhao, R.; Gao, J.; Shi, D. N.; Yang, H. Mechanically Tunable Magnetic Properties of Flexible $SrRuO_3$ Epitaxial Thin Films on Mica Substrates. *Adv. Electron. Mater.* **2018**, *4*, 1700522.
(38) Wu, H.; Sun, H.; Chen, C. F. Superior Magnetic and Mechanical Property of $MnFe_3N$ Driven by Electron Correlation and Lattice Anharmonicity. *Phys. Rev. B* **2015**, *91*, No. 064102.
(39) Gressmann, T.; Wohlschlögel, M.; Shang, S.; Welzel, U.; Leineweber, A.; Mittemeijer, E. J.; Liu, Z. K. Elastic Anisotropy of γ'-Fe_4N and Elastic Grain Interaction in γ'-Fe_4N_{1-y} Layers on α-Fe: First-Principles Calculations and Diffraction Stress Measurements. *Acta Mater.* **2007**, *55*, 5833−5843.
(40) Kokado, S.; Fujima, N.; Harigaya, K.; Shimizu, H.; Sakuma, A. Theoretical Analysis of Highly Spin-Polarized Transport in the Iron Nitride Fe_4N. *Phys. Rev. B* **2006**, *73*, 172410.
(41) Sunaga, K.; Tsunoda, M.; Komagaki, K.; Uehara, Y.; Takahashi, M. Inverse Tunnel Magnetoresistance in Magnetic Tunnel Junctions with an Fe_4N Electrode. *J. Appl. Phys.* **2007**, *102*, No. 013917.
(42) Komasaki, Y.; Tsunoda, M.; Isogami, S.; Takahashi, M. 75% Inverse Magnetoresistance at Room Temperature in Magnetic Tunnel Junctions Fabricated on Cu Underlayer. *J. Appl. Phys.* **2009**, *105*, No. 07C928.
(43) Isogami, S.; Tsunoda, M.; Komasaki, Y.; Sakuma, A.; Takahasi, M. Inverse Current-Induced Magnetization Switching in Magnetic Tunnel Junctions with Fe_4N Free Layer. *Appl. Phys. Express* **2010**, *3*, 103002.
(44) Costa-Krämer, J. L.; Borsa, D. M.; García-Martín, J. M.; Martín-González, M. S.; Boerma, D. O.; Briones, F. Structure and Magnetism of Single-Phase Epitaxial γ'-Fe_4N. *Phys. Rev. B* **2004**, *69*, 144402.
(45) Mi, W. B.; Guo, Z. B.; Feng, X. P.; Bai, H. L. Reactively Sputtered Epitaxial γ'-Fe_4N Films: Surface Morphology, Microstructure, Magnetic and Electrical Transport Properties. *Acta Mater.* **2013**, *61*, 6387−6395.
(46) Kresse, G.; Furthmüller, J. Efficiency of Ab-Initio Total Energy Calculations for Metals and Semiconductors Using a Plane-Wave Basis Set. *Comp. Mater. Sci.* **1996**, *6*, 15−50.
(47) Kresse, G.; Joubert, D. From Ultrasoft Pseudopotentials to the Projector Augmented-Wave Method. *Phys. Rev. B* **1999**, *59*, 1758−1775.
(48) Perdew, J. P.; Burke, K.; Ernzerhof, M. Generalized Gradient Approximation Made Simple. *Phys. Rev. Lett.* **1996**, *77*, 3865−3868.
(49) Daalderop, G. H. O.; Kelly, P. J.; Schuurmans, M. F. H. First-Principles Calculation of the Magnetocrystalline Anisotropy Energy of Iron, Cobalt, and Nickel. *Phys. Rev. B* **1990**, *41*, 11919−11937.
(50) Yin, L.; Wang, X. C.; Mi, W. B. Perpendicular Magnetic Anisotropy Preserved by Orbital Oscillation in Strained Tetragonal $Fe_4N/BiFeO_3$ Bilayers. *ACS Appl. Mater. Interfaces* **2017**, *9*, 15887−15892.
(51) Chen, W. L.; Yan, A.; Wang, C. Y.; Deng, Y.; Chen, D. C.; Xiao, H.; Zhang, D. D.; Meng, X. N. Microstructures and Mechanical Properties of AlCrN/TiSiN Nanomultilayer Coatings Consisting of fcc Single-Phase Solid Solution. *Appl. Surf. Sci.* **2020**, *509*, 145303.
(52) Wang, K.; Dong, S.; Xu, Z. Thickness and Substrate Effects on the Perpendicular Magnetic Properties of Ultra-Thin TbFeCo Films. *Surf. Coat. Tech.* **2019**, *359*, 296−299.
(53) Yu, C. Q.; Li, H.; Luo, Y. M.; Zhu, L. Y.; Qian, Z. H.; Zhou, T. J. Thickness-Dependent Magnetic Order and Phase-Transition Dynamics in Epitaxial Fe-Rich FeRh Thin Films. *Phys. Lett. A* **2019**, *383*, 2424−2428.
(54) Wang, L.; Feng, C.; Cao, M. D.; Meng, F.; Yin, Y. K.; Li, B. H.; Ogata, S.; Geng, W. T.; Yu, G. H. Synergistic Effect of Lattice Strain and Co Doping on Enhancing Thermal Stability in $Fe_{16}N_2$ Thin Film with High Magnetization. *J. Magn. Magn. Mater.* **2020**, *495*, 165873.
(55) Zhang, Y.; Shen, L. K.; Liu, M.; Li, X.; Lu, X. L.; Lu, L.; Ma, C. R.; You, C. Y.; Chen, A. P.; Huang, C. W.; Chen, L.; Alexe, M.; Jia, C. L. Flexible Quasi-Two-Dimensional $CoFe_2O_4$ Epitaxial Thin Films for Continuous Strain Tuning of Magnetic Properties. *ACS Nano* **2017**, *11*, 8002−8009.
(56) Zhang, Y.; Wang, Z.; Cao, J. X. Predicting Magnetostriction of MFe_3N (M=Fe, Mn, Ir, Os, Pd, Rh) from ab Initio Calculations. *Comp. Mater. Sci.* **2014**, *92*, 464−467.
(57) Lord, J. S.; Armitage, J. G. M.; Riedi, P. C.; Matar, S. F.; Demazeau, G. The Volume Dependence of the Magnetization and NMR of Fe_4N and Mn_4N. *J. Phys.: Condens. Matter* **1994**, *6*, 1779−1790.

https://dx.doi.org/10.1021/acsami.0c08042
ACS Appl. Mater. Interfaces 2020, 12, 27394−27404

(58) Arcas, J.; Hernando, A.; Barandiarán, J. M.; Prados, C.; Vázquez, M.; Marín, P.; Neuweiler, A. Soft to Hard Magnetic Anisotropy in Nanostructued Magnets. *Phys. Rev. B* **1998**, *58*, 5193−5196.
(59) Kurtan, U.; Topkaya, R.; Baykal, A.; Toprak, M. S. Temperature Dependent Magnetic Properties of $CoFe_2O_4$/CTAB Nanocomposite Synthesized by Sol-Gel Auto-Combustion Technique. *Ceram. Int.* **2013**, *39*, 6551−6558.
(60) Skomski, R.; Sellmyer, D. J. Anisotropy of Rare-Earth Magnets. *J. Rare Earth* **2009**, *27*, 675−679.
(61) Millis, A. J. Lattice Effects in Magnetoresistive Manganese Perovskites. *Nature* **1998**, *392*, 147−150.
(62) Zhao, J.; He, C. L.; Yang, R.; Shi, Z. W.; Cheng, M.; Yang, W.; Xie, G. B.; Wang, D. M.; Shi, D. X.; Zhang, G. Y. Ultra-Sensitive Strain Sensors Based on Piezoresistive Nanographene Films. *Appl. Phys. Lett.* **2012**, *101*, No. 063112.
(63) Kim, T. K.; Takahashi, M. New Magnetic Material Having Ultrahigh Magnetic Moment. *Appl. Phys. Lett.* **1972**, *20*, 492−494.
(64) Komuro, M.; Kozono, Y.; Hanazono, M.; Sugita, Y. Epitaxial Growth and Magnetic Properties of $Fe_{16}N_2$ Films with High Saturation Magnetic Flux Density (invited). *J. Appl. Phys.* **1990**, *67*, 5126−5130.
(65) Coehoom, R.; Daalderop, G. H. O.; Jansen, H. J. F. Full-Potential Calculations of the Magnetization of $Fe_{16}N_2$ and Fe_4N. *Phys. Rev. B* **1993**, *48*, 3830−3834.
(66) Frazer, B. C. Magnetic Structure of Fe_4N. *Phys. Rev.* **1958**, *112*, 751−754.
(67) Li, Z. R.; Mi, W. B.; Bai, H. L. Electronic Structure, Vibronic Properties and Enhanced Magnetic Anisotropy Induced by Tetragonal Symmetry in Ternary Iron Nitrides: A First-Principles Study. *Comp. Mater. Sci.* **2018**, *142*, 145−152.
(68) Li, Z. R.; Mi, W. B.; Bai, H. L. The Role of Rare-Earth Dopants in Tailoring the Magnetism and Magnetic Anisotropy in Fe_4N. *J. Phys. Chem. Solids* **2018**, *116*, 7−14.
(69) Shen, L. K.; Lan, G. H.; Lu, L.; Ma, C. R.; Cao, C. M.; Jiang, C. J.; Fu, H. R.; You, C. Y.; Lu, X. L.; Yang, Y. D.; Chen, L.; Liu, M.; Jia, C. L. A Strategy to Modulate the Bending Coupled Microwave Magnetic in Nanoscale Epitaxial Lithium Ferrite for Flexible Spintronic Devices. *Adv. Sci.* **2018**, *5*, 1800855.
(70) Takata, F.; Kabara, K.; Ito, K.; Tsunoda, M.; Suemasu, T. Negative Anisotropic Magnetoresistance Resulting from Minority Spin Transport in $Ni_xFe_{4-x}N$ (x=1 and 3) Epitaxial Films. *J. Appl. Phys.* **2017**, *121*, No. 023903.
(71) Kokado, S.; Tsunoda, M.; Harigaya, K.; Sakuma, A. Anisotropic Magnetoresistance Effects in Fe, Co, Ni, Fe_4N, and Half-Metallic Ferromagnet: a Systematic Analysis. *J. Phys. Soc. Jpn.* **2012**, *81*, No. 024705.
(72) Wu, P. C.; Chen, P. F.; Do, T. H.; Hsieh, Y. H.; Ma, C. H.; Ha, T. D.; Wu, K. H.; Wang, Y. J.; Li, H. B.; Chen, Y. C.; Juang, J. Y.; Yu, P.; Eng, L. M.; Chang, C. F.; Chiu, P. W.; Tjeng, L. H.; Chu, Y. H. Heteroepitaxy of Fe_3O_4/Muscovite: A New Perspective for Flexible Spintronics. *ACS Appl. Mater. Interfaces* **2016**, *8*, 33794−33801.

https://dx.doi.org/10.1021/acsami.0c08042
ACS Appl. Mater. Interfaces 2020, 12, 27394−27404